Magn Reson Med Sci 2023; 22; 103–115
doi:10.2463/mrms.tn.2021-0094 Published Online: December 10, 2021

TECHNICAL NOTE

Development of an Add-on ^{23}Na-MRI Radiofrequency Platform for a ^{1}H-MRI System Using a Crossband Repeater: Proof-of-concept

Michiru Kajiwara[1], Tomoyuki Haishi[2,3,4], Dwi Prananto[4,5], Susumu Sasaki[4,5], Ryohei Kaseda[4,6], Ichiei Narita[4,6], and Yasuhiko Terada[1*]

^{23}Na-MRI provides information on Na^+ content, and its application in the medical field has been highly anticipated. However, for existing clinical ^{1}H-MRI systems, its implementation requires an additional broadband RF transmitter, dedicated transceivers, and RF coils for Na^+ imaging. However, a standard medical MRI system cannot often be modified to perform ^{23}Na imaging. We have developed an add-on crossband RF repeater system that enables ^{23}Na-MRI simply by inserting it into the magnet bore of an existing ^{1}H MRI. The three axis gradient fields controlled by the ^{1}H-MRI system were directly used for ^{23}Na imaging without any deformation. A crossband repeater is a common technique used for amateur radio. This concept was proven by a saline solution phantom and *in vivo* mouse experiments. This add-on RF platform is applicable to medical ^{1}H MRI systems and can enhance the application of ^{23}Na-MRI in clinical usage.

Keywords: *add-on platform, crossband repeater, live mouse imaging, sodium magnetic resonance imaging*

Introduction

Conventional MRI systems visualize ^{1}H nuclei in biological tissues and are widely used for clinical diagnosis and research. With the recent technical improvements (e.g., higher magnetic field strengths and improved gradient hardware and sequences), X-nuclei (non-proton) MRI has attracted much attention. X-nuclei MRI (e.g., ^{13}C, ^{17}O, ^{23}Na, ^{35}Cl, ^{31}P, and ^{39}K nuclei MRI) provides metabolic information on ions metabolism and homeostasis *in vivo*, which cannot be detected by traditional ^{1}H-MRI, and thus has the potential of being a tool for precise diagnosis and for clarifying physiological milieu.[1] ^{23}Na has a high natural abundance and high concentration in the body. In addition, ^{23}Na has short relaxation times, which allows for fast imaging with a large flip angle. For these reasons, ^{23}Na-MRI signals can be obtained with relatively high sensitivity, and many studies have been performed with ^{23}Na imaging. The value of ^{23}Na-specific applications in the kidney,[2–5] brain,[6] multiple sclerosis,[7,8] stroke,[9] heart,[10,11] muscle, and brain,[12] as well as knee,[13] has been shown.

Conventional clinical MRI systems for 1.5 Tesla or 3 Tesla are optimized for ^{1}H imaging with narrow-band RF digital electronics working at the ^{1}H resonance frequency. Thus, ^{23}Na or other X-nuclei imaging cannot be performed with the conventional MRI without additional hardware (transceiver and spectrometer, RF transmitter, RF coils, etc.) corresponding to the resonance frequency of the specific target nucleus. For this additional purpose for medical research, a broadband multinuclear spectroscopy (MNS) package that works at the resonance frequencies of multiple X-nuclei is commercially available only for high-end medical MRI systems or research MRI systems. There is another type of signal transceiver that uses frequency conversions between the resonance frequencies of ^{1}H and the X-nucleus.[14] Dedicated RF coils and an RF transmitter are also needed to transmit and receive X-nucleus signals. To this end, multiresonant RF coils[14,15] are often employed, but the design of multi-tuned RF coils resonating at even two frequencies has unavoidable disadvantages because their sensitivity tends to be inferior to that of single-tuned coils. The design of double-tuned RF coils for X-nuclei is reviewed in Ref. 16.

[1]Institute of Applied Physics, University of Tsukuba, Tsukuba, Ibaraki, Japan,
[2]Department of Radiological Sciences, School of Health Sciences at Narita, International University of Health and Welfare, Narita, Chiba, Japan
[3]MRTechnology Inc., Tsukuba, Ibaraki, Japan
[4]Japan Agency for Medical Research and Development, AMED SENTAN, Tokyo, Japan
[5]Faculty of Engineering, Niigata University, Niigata, Niigata, Japan
[6]Division of Clinical Nephrology and Rheumatology, Niigata University, Niigata, Niigata, Japan

*Corresponding author: Institute of Applied Physics, University of Tsukuba, 1-1-1, Tennodai, Ibaraki 305-8573, Japan. Phone: +81-29-853-5214, Fax: +81-29-853-5769, Email: terada@bk.tsukuba.ac.jp

Received: June 29, 2021 | Accepted: October 13, 2021

Several advanced research facilities have the MNS package and appropriate hardware on their clinical scanners. However, ^{23}Na-MRI has not been available in clinical practice because of the high cost and the poor availability of dedicated hardware setups, such as the additional ^{23}Na transmitter and RF coils. Once a clinical MRI system is installed solely for ^{1}H imaging, the system configuration cannot be modified to ^{23}Na-MRI until the next major reinstallation. These additional costs are a major obstacle to further development for clinical applications of ^{23}Na-MRI.

Another challenge is that the MNS package cannot technically be installed into a standard or low-end MRI system, and the only way to perform ^{23}Na-MRI is to replace the entire system. However, the lifespan of the MRI system is generally more than 10 years, making it difficult to replace frequently.

To address these issues, here we developed a novel add-on ^{23}Na-MRI RF platform consisting of a crossband repeater (CBR), which is an amateur radio technology, with a low-band RF transmitter to pick up and transmit coils. Three axis gradient fields controlled and applied from a ^{1}H-MRI scanner can be directly used for ^{23}Na imaging. The proposed add-on RF platform can be installed into existing 1.5 or 3 Tesla ^{1}H-MRI scanners without modifying the parent scanner configuration at minimal cost, and thus enables ^{23}Na-MRI with the standard ^{1}H scanners. Most of the existing systems use RF equipment operating at a single frequency, and thus, equipment needs to be added for transmission and reception to control and observe the second set of RF signals synchronously. In contrast, this system can be realized at a low cost because it uses ^{1}H RF equipment for the transmission and reception of the second set of RF signals. The add-on RF platform can also be shared with different scanners at the same site or at a neighboring site, or targeting other nuclei like ^{31}P, thus reducing the total hardware cost and promoting its usability. This study presents an initial proof-of-concept for an add-on ^{23}Na-MRI platform to a 1.5 T ^{1}H scanner, followed by its application to *in vivo* imaging of a live mouse. The concept of the proposed RF platform is applicable to other ^{1}H scanners and would expand the opportunity for researchers to assess the clinical applications of ^{23}Na-MRI.

Add-on ^{23}Na-MRI RF platform

Concept and operating principle

A schematic diagram of the proposed add-on ^{23}Na platform built into a conventional 1.5 Tesla ^{1}H-MRI system is presented in Fig. 1a. The add-on RF platform consists of a ^{23}Na birdcage RF transmit and receive coils, loop pickup and transmit coils, a ^{1}H-RF shield, and a CBR system. The loop pickup and transmit coils were used to receive and transmit ^{1}H-RF pulses from or to the ^{1}H system. The ^{1}H-RF shield was used to shield the ^{23}Na-RF coil and sample from the ^{1}H transmitted pulse. The CBR system was mainly used to convert the signals between ^{1}H- and ^{23}Na-NMR frequencies (f_p and f_s). At the B_0 field strength of 1.5 Tesla, the ^{1}H frequency is about 64 MHz and the ^{23}Na frequency is about 17 MHz. For ^{23}Na imaging, the RF probe head of the add-on platform was inserted into the imaging bore in the transmission coil of the ^{1}H-MRI system. For ^{1}H, the probe head of the add-on RF platform was removed from the imaging bore.

The operating principle of ^{23}Na imaging is as follows. Briefly, a ^{1}H-RF pulse is emitted from the ^{1}H system and is detected by the loop pickup coil of the CBR. Next, the CBR down-converts the ^{1}H pulse (modulated at f_p) to the ^{23}Na frequency, and the ^{23}Na pulse (modulated at f_s) is used to excite the sample with the birdcage ^{23}Na RF coil. Instead of the birdcage-type coil, a loop coil can also be used. The excitation pulse amplitude should be carefully adjusted. Because the gyromagnetic ratio for ^{23}Na is about 1/4 of the ^{1}H proton, specific absorption ratio (SAR) is not severe when the small local ^{23}Na transmission coil is used. The resulting ^{23}Na-MRI signal from the imaging sample is received by the same ^{23}Na RF coil, transferred to the CBR, up-converted to f_p, and transmitted back with the loop-transmit coil to the birdcage ^{1}H-RF coil. In summary, the ^{1}H system receives the ^{23}Na-MRI signal converted at the ^{1}H resonant frequency by the CBR.

More specifically (Fig. 1b), the CBR consists of an RF transmitter, a transmit and receive (TX/RX) switch, a low-noise amplifier (LNA), and a crossband converter. The transmitted ^{1}H-pulse signal is picked up, divided, and transferred to a gate generator and a frequency mixer I in the crossband converter. The generated gate pulse is used to control the timing of the RF pulse transmission and the TX/RX switch. The transmitted ^{1}H pulse (modulated at f_p) is mixed with the signal from a local oscillator (with the oscillation frequency $f_{LO} = f_p - f_s$) in the frequency mixer I. The modulated pulse (at $f_p \pm f_{LO}$) passes through a low-pass filter (LPF) to output the signal for the ^{23}Na transmit RF pulse (modulated at $f_s = f_p - f_{LO}$), and is transferred to the RF transmitter. The ^{23}Na birdcage coil transmits the ^{23}Na RF pulse and receives the ^{23}Na-MR signal from the sample. The ^{23}Na-MR signal (modulated at f_s) is pre-amplified by the LNA, up-converted to the ^{1}H resonance frequency (f_p) with the frequency mixer II and an LPF, and amplified by another LNA. The up-converted ^{23}Na-MR signal is transmitted to the birdcage ^{1}H-RF coil of the ^{1}H system and is detected by the ^{1}H system. To this end, the ^{1}H system receives the ^{23}Na-MRI signal without recognizing it as being the frequency-converted signal by the CBR. The ^{1}H-MRI system works as if the ^{1}H birdcage coil transmitted and received the ^{1}H signal, but what was transmitted and received was the ^{23}Na signal modulated by the ^{1}H resonance frequency. Since the gyromagnetic ratio for ^{23}Na is about 1/4 of the ^{1}H proton, the FOV of the ^{23}Na becomes 4 times wider than original ^{1}H proton's MRI sequence.

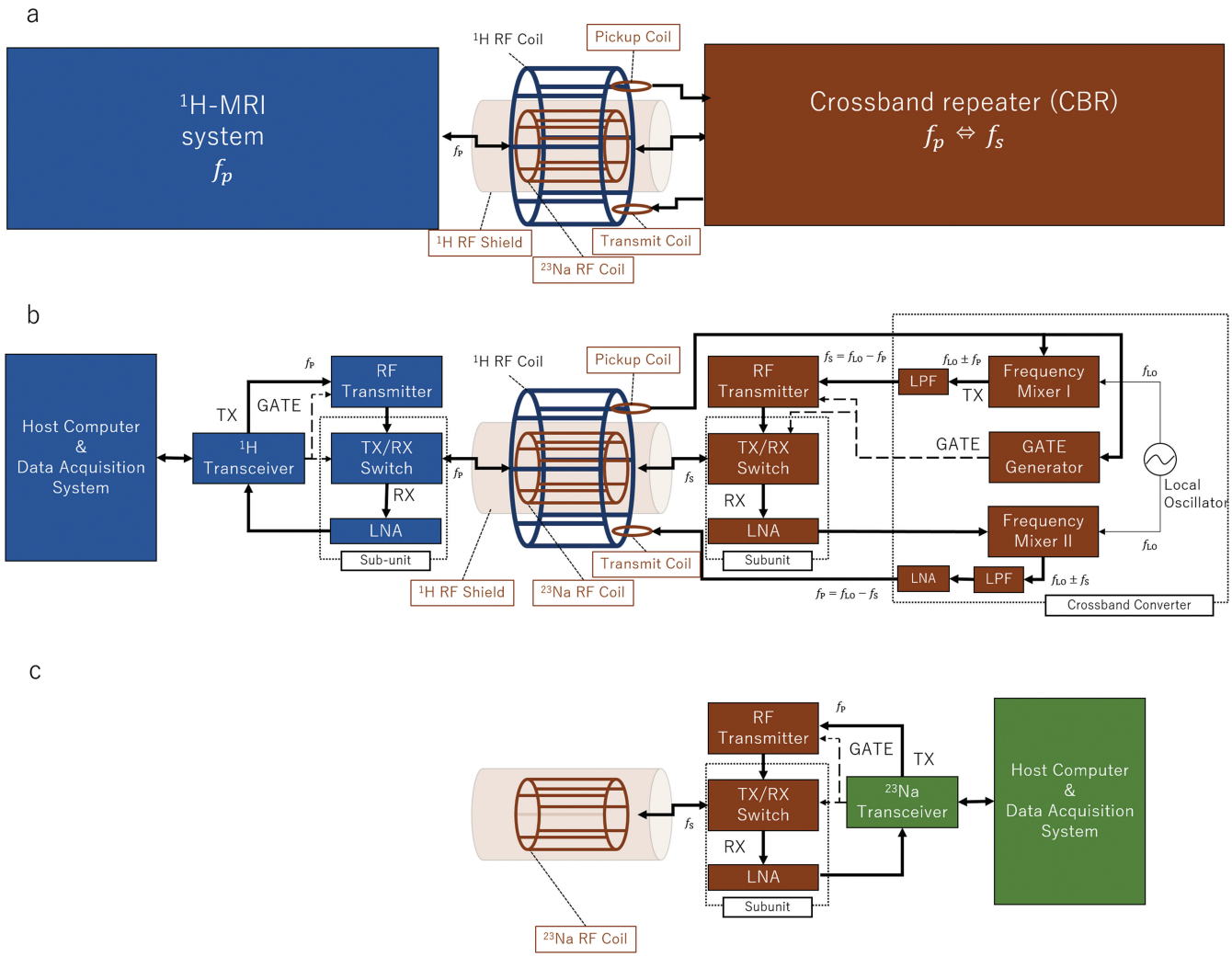

Fig. 1 Block diagrams of the add-on platform using the CBR. (**a** and **b**) The add-on ^{23}Na/^{1}H-MRI system. (**c**) Conventional ^{23}Na-MRI system. CBR, crossband repeater; LNA, low-noise amplifier; LPF, low-pass filter; RX, receive; TX, transmit.

Setup

The add-on ^{23}Na RF platform equipped with a conventional ^{1}H-MRI system is shown in Fig. 2. The ^{1}H-MRI system consisted of a 1.5 T superconducting magnet with a 280 mm bore (JMBT-1.5/280/SS; JASTEC, Hyogo, Japan), a home-built birdcage RF transmit and receive coil for ^{1}H (Fig. 2f), a home-built shielded gradient coil, an RF transmitter (150 W, 64 MHz; DST, Saitama, Japan), a three-axis gradient driver (20 V, 20 A; DST), a digital MRI transceiver for ^{1}H (DTRX6; MRTechnology, Ibaraki, Japan),[17] a digital subunit consisting of a preamplifier and a TX/RX switch (64 MHz; DST), and a Windows PC. The resonance frequencies for ^{1}H (f_p) and ^{23}Na (f_s) were 63.903 and 16.908 MHz, respectively. The imaging volume was 10 cm diameter-sphere-volume (DSV). The maximum field gradient was 14.9 mT/m.

The add-on RF platform consisted of the CBR, ^{1}H-RF shield, and RF coils. The CBR consisted of an RF transmitter (500 kHz–150 MHz, 2 kW, BTO2000-AlphaSA; TOMCO, Stepney, Australia), a crossband converter (16–64 MHz; MRTechnology), and a digital subunit consisting of a pre-amplifier and a TX/RX switch (17 MHz; DST). A picture and a block diagram of the crossband converter are shown in Fig. 3.

The RF coil assembly is shown in Fig. 2b and 2c. The ^{1}H birdcage RF coil was located at the outermost side, and the ^{1}H pickup and transmit coils, ^{1}H-RF shield, ^{23}Na birdcage RF coil, and the sample were placed in this order toward the inner side. The ^{1}H birdcage coil was a part of the ^{1}H-MRI system, and its coil diameter and length were 110 and 130 mm, respectively.

Other RF coils were prepared in this study; the pickup and transmit coils (Fig. 2d and 2e, respectively) were tuned and matched to f_p. These were two-loop coils of 50 and 45 mm diameter. After construction, they were slightly bent and attached with Kapton tape to the ^{1}H-RF shield. The configurations of pickup and transmit coils were optimized in

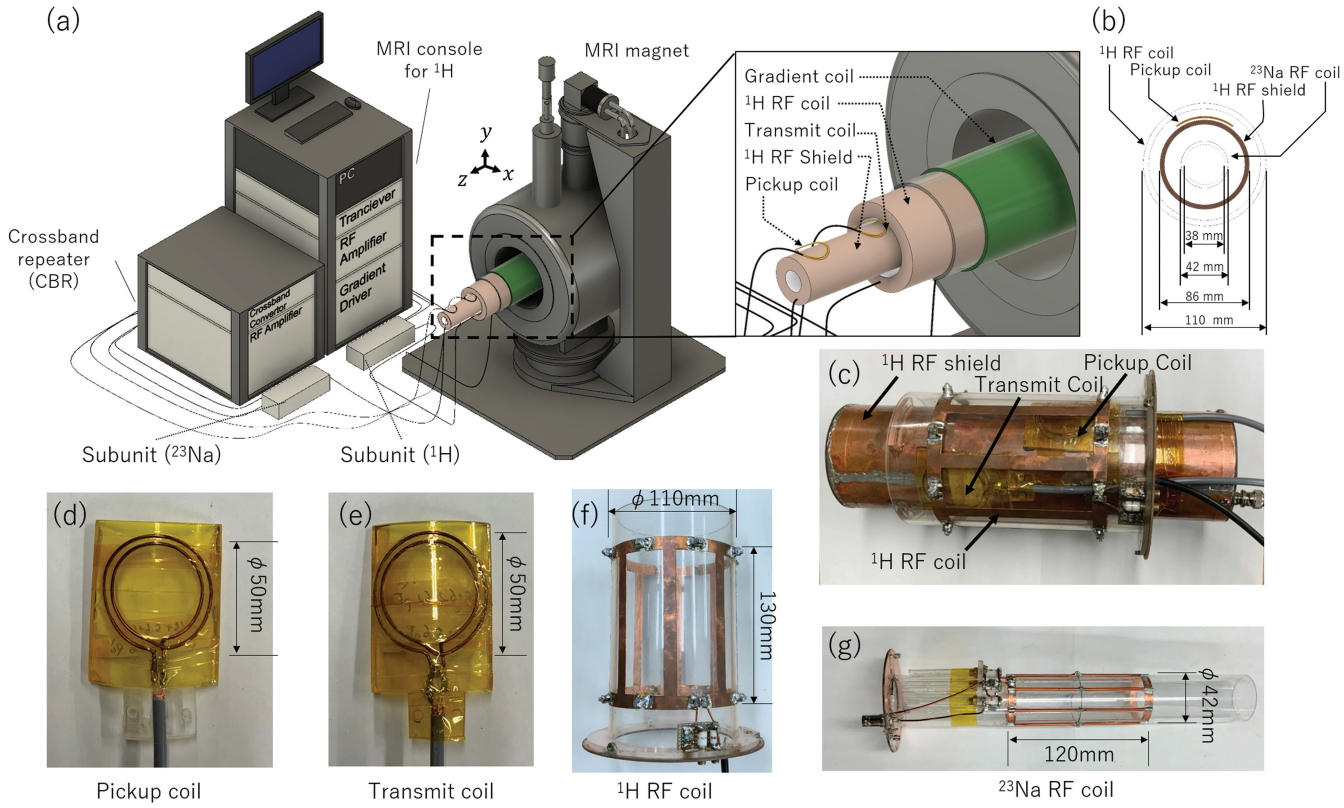

Fig. 2 Add-on ^{23}Na-MRI platform equipped with the 1.5 T ^{1}H system. (**a**) Schematic overview of the system. (**b** and **c**) RF coil assembly. (**d**) Pickup coil. (**e**) Transmit coil. (**f**) ^{1}H-RF coil (without the shield). (**g**) ^{23}Na RF coil (without the shield). CBR, crossband repeater.

advance using a commercial electromagnetic simulator (FEKO, www.feko.info) so that the transfer functions between the pickup coil and ^{1}H-RF coil and that between the transmit coil and ^{1}H RF coil were maximized. (See Supplementary Information for the optimization details).

The ^{1}H-RF shield was designed in a way that the shielding isolation efficiency was more than 60 dB inside the shield. The shielding efficiency was calculated with FEKO (see Subsection of Shield efficiency of ^{1}H-RF shield in Materials and Methods). It was constructed by wrapping 100-μm-thick copper sheets inside and outside an acrylic pipe (300 mm long, 86 mm outer diameter, and 80 mm inner diameter).

We also constructed a ^{23}Na RF coil (Fig. 2g) tuned and matched to f_s. It was a low-pass birdcage coil (6 legs, 42 mm in diameter, and 120 mm in length). The end-ring was made of copper sheet (100 um thick and 6 mm wide), the leg was made of copper wire (2 mm in diameter), and they were fixed on an acrylic cylinder. The ^{23}Na-RF coil was fixed to the ^{1}H-RF shield with stainless steel screws and acrylic spacers. The Q values of the ^{1}H and ^{23}Na coil were 137/118 and 82.2/67.0 (unloaded/loaded), respectively.

Comparison with conventional ^{23}Na system

A conventional ^{23}Na system (Fig. 1c) was used to compare the performance with the add-on system. The conventional ^{23}Na system consisted of a ^{23}Na birdcage RF coil, ^{23}Na RF transmitter, gradient driver, gradient coils, and a digital sub-unit (the same devices as used in the add-on system), and consisted of a digital MRI transceiver for ^{23}Na (DTRX6; MRTechnology) and a Windows PC (that were used only in the conventional ^{23}Na system).

Materials and Methods

Bench test of control signals

The RF fidelity and time response of the control signals were measured using an oscilloscope (2 GHz, ViewGo II; Iwatsu, Tokyo, Japan). The measured signals were as follows: a ^{1}H transmitted RF pulse and a gate pulse from the ^{1}H system, a pulse acquired by the ^{1}H pickup coil, a ^{23}Na transmitted RF pulse, and a gate pulse from the add-on system. The transmission power gain of ^{23}Na was proportional to the detected ^{1}H transmission power, and the gain was carefully chosen not to apply an overpowered RF of ^{23}Na pulse more than the SAR limit of ^{1}H pulse. The local ^{23}Na RF coil was small enough compared with the ^{1}H body coil installed in the outermost diameter of the MRI's imaging bore.

Shield efficiency of ^{1}H-RF shield

The shielding isolation efficiency was evaluated with a FEKO simulator. The maps of the magnetic field B_1

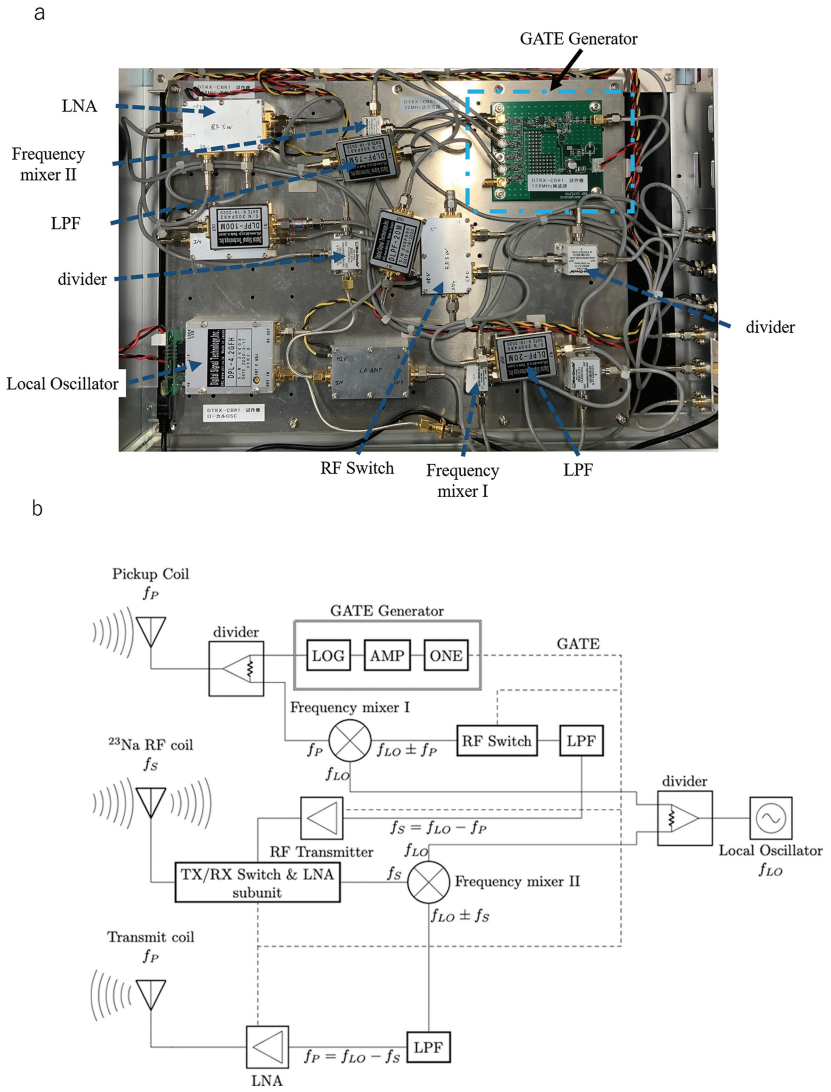

Fig. 3 Crossband converter. (**a**) Crossband converter unit. (**b**) Block diagram. AMP, amplifier; LNA, low-noise amplifier; LOG, logarithmic; LPF, low-pass filter; ONE, one-shot circuit; RX, receive; TX, transmit.

generated by the ^{1}H birdcage coil was calculated in the center area with and without the RF shield, and the shielding efficiency map was calculated from the ratio of the two maps. The evaluated areas were an *xy* plane (axial plane, 150 mm × 150 mm) and an *xz* plane (coronal plane, 150 mm × 200 mm), where *z* was the B_0 direction (Fig. 2a).

Sensitivity measurement

To evaluate the sensitivity of the ^{23}Na signals, the free induction decay (FID) signal from a saline phantom was measured in the following three cases: (A) using the conventional ^{23}Na system (for reference), (B) using the add-on system, and (C) using the add-on system with a direct bypass electrical connection (DEC) from the crossband converter (the LNA after the LPF) to the ^{1}H-MRI transceiver using a coaxial cable with Bayonet Neill-Concelman (BNC) connectors, instead of connecting via electromagnetic coupling between the transmit coil and the birdcage coil of the ^{1}H system. Experiment C was performed to evaluate the RF signal loss in the electromagnetic coupling between the two ^{1}H-RF coils.

The temporal signal intensity was measured from the FID magnitude, 140 μs after the excitation pulse applied with the saline phantom. The relative signal loss was calculated from the signal intensity and the total receiver gain.

The phantom consisted of 19.4 cm^3 of a saturated saline solution and 7.0 cm^3 purified water (Fig. 4). Here, the saturated saline solution was the only source of the ^{23}Na-MR signal because there are no ^{23}Na nuclei in pure water. This was indeed confirmed by the imaging (see Subjection of Phantom imaging in Results).

Phantom imaging

The saline phantom described above was also used for imaging measurement. The image sequences were 3D,

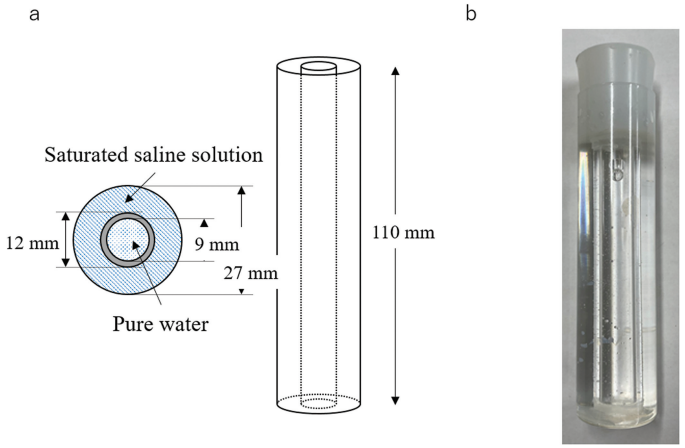

Fig. 4 Phantom consisting of saturated saline solution and pure water. (**a**) Schematic view. (**b**) Photograph.

coronal, and axial gradient-echo sequences. The detailed parameters are listed in Table 1. The 90 degrees of flip angle was determined under the condition that the FID signal is maximized. The signal was integrated four times to increase the image SNR. The image SNR was measured by dividing the mean signal level over a given area in saturated saline solution by the standard deviation of the signal level in an outside area.

In vivo MR imaging

For *in vivo* imaging, an 11-week-old mouse (C57BL/6J, Male) was imaged under gas anesthesia. The anesthesia was administrated by isoflurane with a gas anesthesia system (MRTechnology). The sequence parameters are listed in Table 2. We used compressed sensing (CS) encoding[18] to shorten the scan time for ^{23}Na mouse imaging, and the acceleration factor was 3.

Due to the configuration difference between the 1.5 Tesla ^{1}H-MRI and the add-on MRI systems, when switching the target configuration between the two systems, repositioning of the mouse from the bore was required. This led to misalignment in the mouse position in the ^{1}H- and ^{23}Na-MR images. To remedy this problem, saline solution markers were placed close to the mouse to guide the alignment of these images.

We also calculated the fused image of the ^{1}H and ^{23}Na images. Since the matrix sizes of the ^{1}H and ^{23}Na images differed by a factor of almost 4, zero-interpolation filling was used to match their matrix sizes. The image SNRs were calculated in the saline and bladder regions.

All experiments and procedures were approved by our Institutional Animal Care and Use Committee.

Results

Bench test of control signals

The measured control signals are shown in Fig. 5. The ^{1}H pickup coil waveform (Fig. 5b) was almost perfectly synchronized with the waveform of the ^{1}H transmitted pulse (Fig. 5a). The ^{23}Na transmitted pulse waveform (Fig. 5c) was modulated at f_s frequency in synchronization with the ^{1}H transmitted pulse. The gate pulse for ^{23}Na-MRI (Fig. 5e) was also synchronized with that for ^{1}H-MRI (Fig. 5d). The delay time for the rising edge of the ^{23}Na gate pulse was about 3 μs, and that of the falling edge was about 0.8 μs. The ^{23}Na transmitted pulse signal was only transmitted, while the ^{23}Na gate was ON.

Effect of ^{1}H-RF isolation shield

The B_1 and RF shielding efficiency maps calculated by the electromagnetic field simulation are shown in Fig. 6. Here, the outer and inner dotted lines indicate the ^{1}H-RF isolation shield and ^{23}Na birdcage RF coil, respectively. The shielding efficiency inside the ^{1}H-RF shield was about 63 dB (the mean was 58 dB in the axial plane and 68.2 dB in the coronal plane), and that inside the ^{23}Na RF coil was about 94 dB (the mean was 100 dB in the axial plane and 88.3 dB in the coronal plane).

Sensitivity measurement

The ^{23}Na-FID signals acquired with the three setups (A–C) (see Subsection of Sensitivity measurement in Materials and Methods) are shown in Fig. 7. The FIDs decayed with the decay time (T_2^*) of 5 ms. The sensitivity results are summarized in Table 3. The signal intensity for the add-on system was –78.6 dBm (–104 dBm/cm^3 for the saturated saline solution), which was close to the result from the conventional ^{23}Na-MRI system (–79.0 dBm, –105 dBm/cm^3 for saturated saline solution). Compared with the conventional ^{23}Na system, the relative signal loss in the add-on system was 21.1 dB, and that in the add-on system with DEC was 9.1 dB.

Phantom imaging

^{1}H and ^{23}Na images of the saline phantom are shown in Fig. 8. The ^{23}Na images were acquired with both the add-on system (Fig. 8b) and the conventional ^{23}Na-MRI system (Fig. 8c). In the ^{1}H image, both the saturated saline solution

Table 1 Sequence parameters used for phantom imaging (3D, SE, and GE)

	^{1}H-MRI coronal 3D-SE	^{1}H-MRI axial 3D-SE	^{23}Na-MRI coronal 3D-GE	^{23}Na-MRI axial 3D-GE
TR (ms)	500	500	40	40
TE (ms)	15	15	2.8	2.8
DW (μsec)	40	40	35	70
FA (deg)	90	90	90	90
FOV (cm^3)	14×7×7	7×7×14	14×7×7	7×7×14
Matrix size	128×64×64	64×64×64	64×32×32	32×32×32
NEX	1	1	4	4
Scan time	34 min 13 s	34 min 13 s	2 min 44 s	2 min 44 s

DW, dwell time: FA, flip angle: GE, gradient echo; NEX, number of excitations: SE, spin echo.

Table 2 Sequence parameters used for *in vivo* imaging (3D, SE, and GE)

	^{1}H-MRI coronal 3D-SE	^{23}Na-MRI coronal 3D-GE
TR (ms)	40	40
TE (ms)	15	2.8
DW (μsec)	40	35
FA (deg)	90	90
FOV (cm^3)	14×7×7	14×7×7
Matrix size	256×128×64	64×32×32
NEX	1	256
Acceleration factor	1	3
Scan time	5 min 36 s	58 min 12 s

DW, dwell time: FA, flip angle: GE, gradient echo; NEX, number of excitations: SE, spin echo.

and pure water were imaged, whereas in the ^{23}Na images, the saturated saline solution was imaged with high intensity, and pure water was not almost visible. Two faint lines may be seen in the inner region of purified water in the coronal image. These would be truncation artifacts because of the limited matrix size.

The image SNRs are listed in Table 4. The image SNRs for the add-on system were comparable to those for the conventional ^{23}Na-MRI system setting.

In vivo study

^{1}H and ^{23}Na images of the live mouse are shown in Fig. 9. In the ^{1}H image, the lungs, bladder, and intestines were visualized. The ^{23}Na images acquired with the add-on RF platform showed bright spots around the bladder, kidney, and saline markers, and the image quality was almost the same as the ^{23}Na images acquired with the conventional ^{23}Na system setting.

The image SNRs are shown in Table 5. As in the phantom study, the image SNRs for both the systems were almost the same.

Discussion

In this study, we developed and evaluated an add-on RF platform that enables ^{23}Na-MRI without any modification to an existing ^{1}H-MRI system. The benchmark result revealed that the control signals generated in the add-on RF platform had high fidelity, and the transmit and gate pulses for ^{23}Na-MRI could be generated synchronously with the ^{1}H-MRI system. The performance of the add-on RF platform was confirmed by the ^{23}Na-MRI images of the saline water phantom and live mouse with high SNRs, which is comparable to the conventional system setting. The results are discussed in detail below.

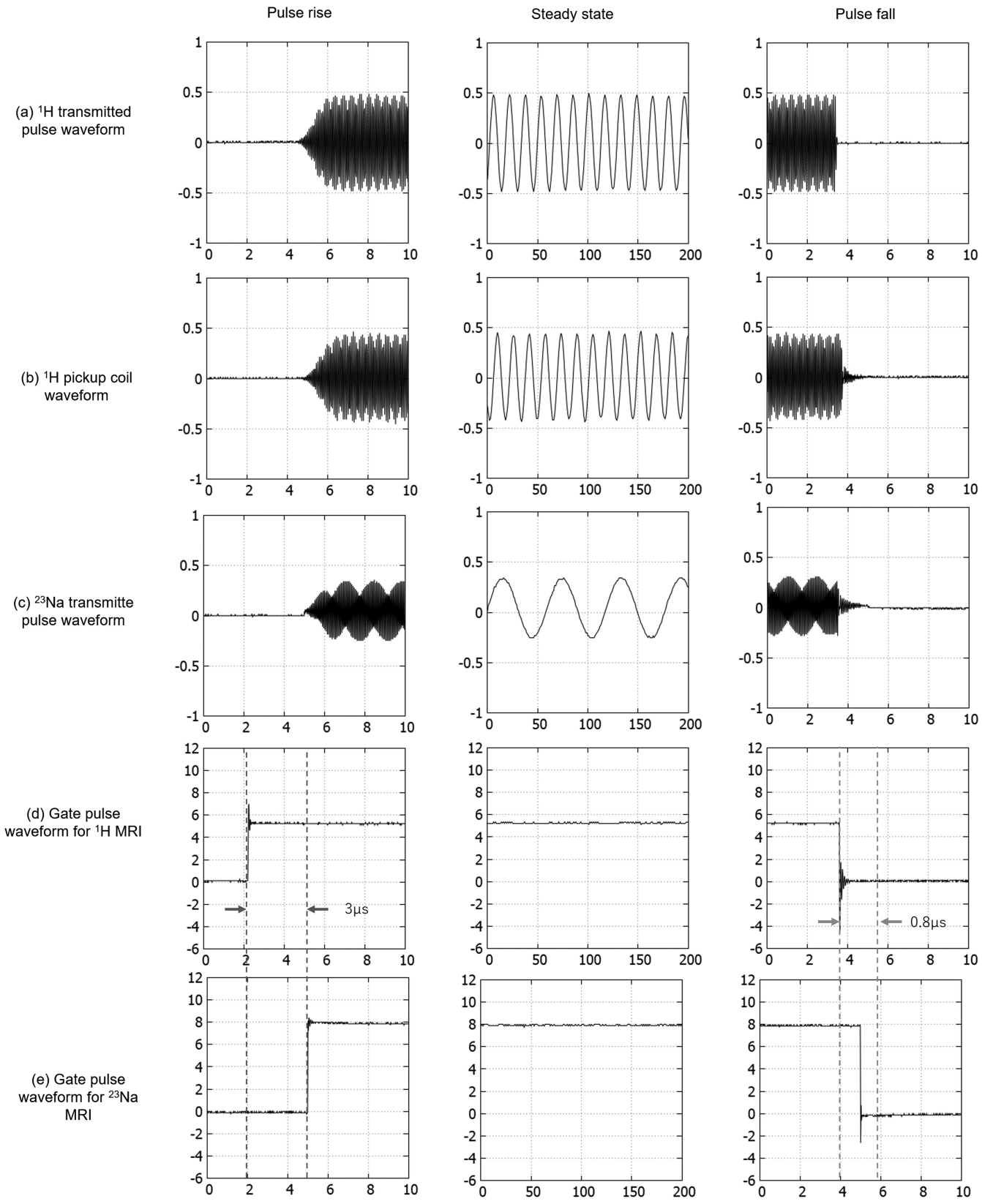

Fig. 5 Waveforms of control signals. (**a**) ^{1}H transmitted pulse waveform. (**b**) ^{1}H pickup coil waveform. (**c**) ^{23}Na transmitted pulse waveform. (**d**) Gate pulse waveform for ^{1}H-MRI. (**e**) Gate pulse waveform for ^{23}Na-MRI.

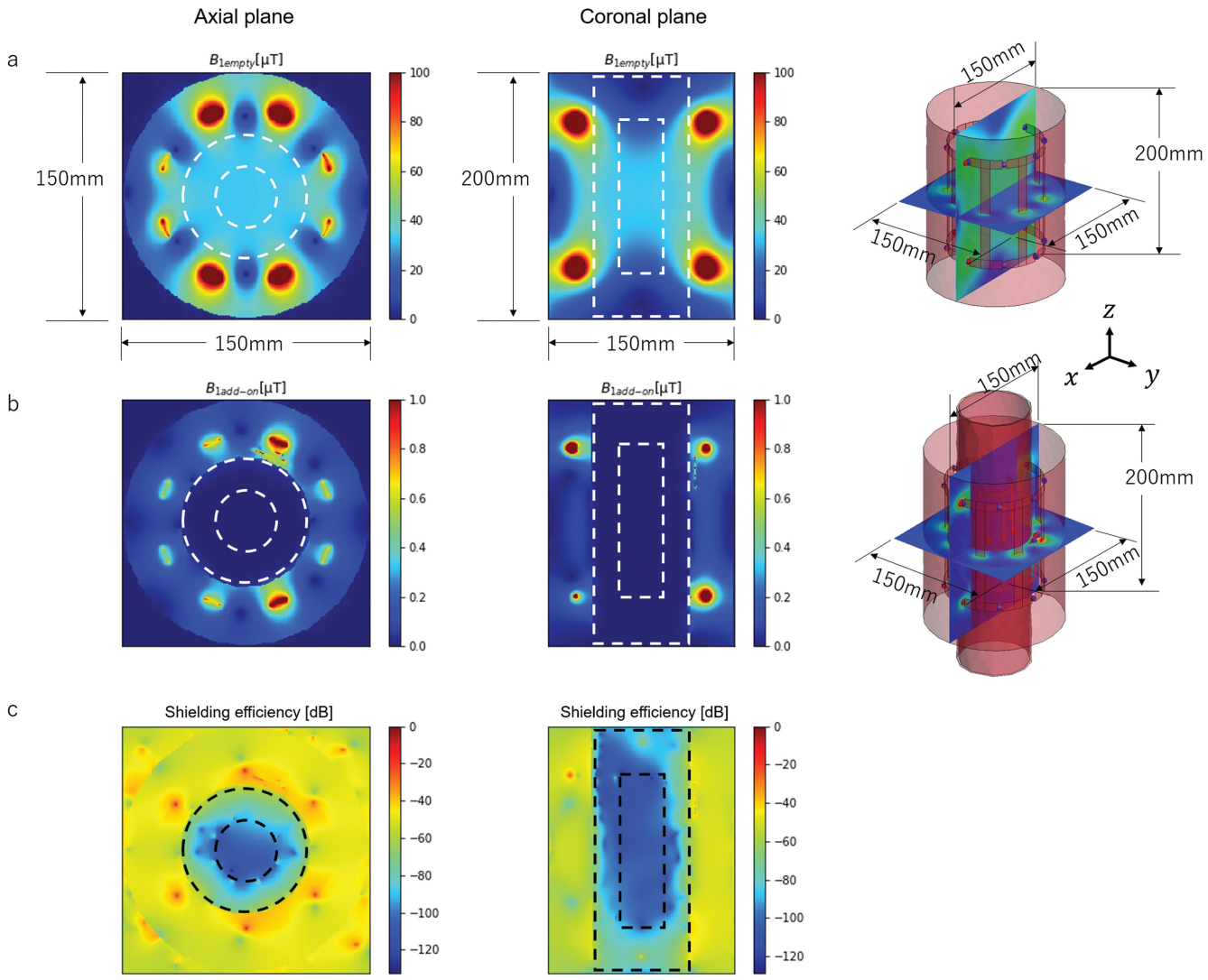

Fig. 6 B_1 generated by the ^{1}H birdcage RF coil and shielding efficiency maps. (**a**) B_1 maps with the ^{1}H-RF shield. (**b**) B_1 maps without the ^{1}H-RF shield. (**c**) Shielding efficiency maps.

The observed control signal waveforms generated in the add-on system showed high fidelity: the delay times for the rising and falling edges of the ^{23}Na gate pulse were only a few μs, which was short enough compared with a typical RF pulse width of 120 μs and had little effect on the operation of the add-on system. The reason that the control waveform could be generated with such a short delay time is that only analog, not digital, processing was performed in the add-on system; digital processing is prone to longer delays.

While performing ^{23}Na-MRI using the add-on system, it was necessary to prevent the sample from being irradiated by the ^{1}H RF transmitted (excitation) pulse generated by the ^{1}H system. For this purpose, we designed a ^{1}H-RF isolation shield, which was shown to have a shielding efficiency of more than 60 dB. In the ^{23}Na image of the phantom, purified water that did not contain ^{23}Na was not imaged. These results indicate that the shielding performance of the add-on system was sufficiently high.

There was also a concern that the transmission and reception signals of ^{1}H and ^{23}Na might be mixed in the add-on system. For example, there might be coupling between the pickup and transmit coils, and interference between ^{1}H and ^{23}Na frequencies in the crossband converter. However, the saline water phantom imaging result showed that these possibilities were negligible and the separation of the ^{1}H and ^{23}Na transmitting and receiving systems worked well as designed.

The signal loss in the add-on system (21.1 dB) was dominated by the loss in the crossband converter (9.1 dB) and the loss in the electromagnetic coupling between the transmit coil and the ^{1}H birdcage coil (12.0 dB). The most

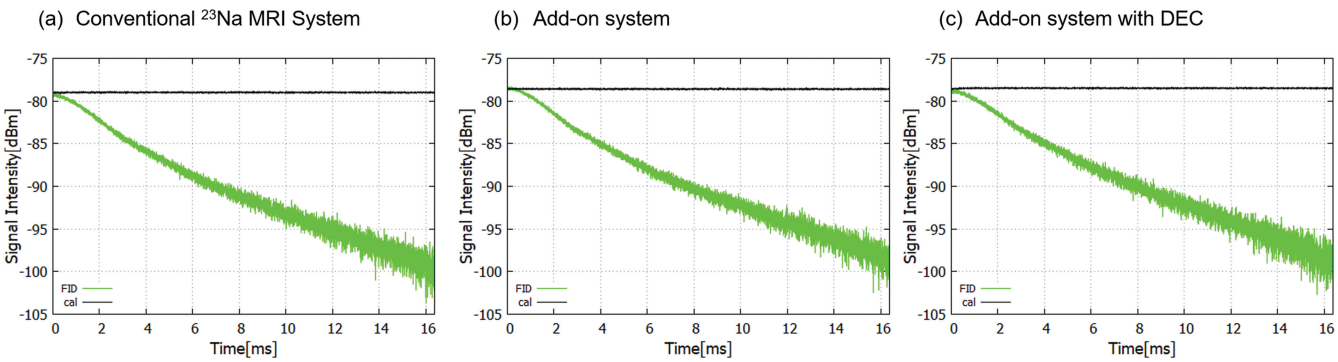

Fig. 7 ^{23}Na FID signals from the phantom. (**a**) Conventional ^{23}Na-MRI system. (**b**) Add-on system. (**c**) Add-on system with DEC. The black lines indicate the estimated signal levels. DEC, direct bypass electrical connection; FID, free induction decay.

Table 3 Signal intensity and loss measured from the FID measurement (DEC, from the crossband converter to the ^{1}H-MRI system)

System	Signal intensity [dBm]	Total receiver gain [dB]	Relative signal loss compared with A [dB]
Conventional ^{23}Na-MRI System (A)	–79.0	83.7	-
Add-on system (B)	–78.6	104.4	21.1
Add-on system with DEC (C)	–78.5	92.3	10.9

DEC, direct bypass electrical connection; FID, free induction decay.

likely sources of loss in the crossband converter are the frequency mixers and LPFs. Based on the datasheet, the loss in the frequency mixer was about 6.5 dB. The loss in the LPF is unknown, but a standard LPF attenuates the signal by only a few dB. Most of the remaining loss occurred in the electromagnetic coupling, and the total signal loss might be improved by optimizing the coil layout to transmit the signal more efficiently.

Despite the larger signal loss compared with the conventional ^{23}Na system setting, the add-on rf platform provided ^{23}Na images with a high SNR, which is comparable to the conventional system setting. Based on Friis's formula, when the gain of the first-stage amplifier (preamp) is sufficiently high, the SNR of the final signal is determined by the SNR of the input signal and the noise figure (NF) of the first-stage amplifier. This was the case in this study, and the signal loss was compensated by the LNA used as the first-stage amplifier, which had a high NF with little additional noise.

The detection limit of the Na concentration is determined by the coil sensitivity, the NF, and sequence, and can be roughly estimated from the condition that the image SNR is 1. The image SNR was 32.0 dB (Table 4) for the saturated saline phantom with a concentration of approximately 26 wt%. Since the Na signal intensity is proportional to the Na concentration, the concentration at which the SNR is 1 is estimated to be 1 wt%, which gives a typical detection limit. The concentration of Na in the kidney is higher than that of saline (0.9 wt%) and the estimated detection limit.

In the *in vivo* mouse imaging measurements, strong signals of ^{23}Na were detected in the kidney and bladder. This is consistent with previous studies showing that ^{23}Na tends to accumulate in these regions.[3,19] Live mouse ^{23}Na imaging has important roles for preclinical studies, and this result indicates that our system can contribute to these applications.

In this study, we used CS undersampling and signal integration to improve the intrinsically low SNR of the ^{23}Na signal. If the SNR is still too low, CS reconstruction may not work well because of the failure of denoising. However, we confirmed that this was not the case by comparing the CS reconstructed image with the zero-fill image (not shown here).

The following issues should be noted when converting the developed add-on RF platform to other ^{1}H-MRI systems. First, it may be necessary to make new ^{1}H pickup and ^{23}Na transmit and receive coils. This is because the S-parameters may change depending on the coil configuration and the resonance frequency of the target ^{1}H system. This issue is more remarkable when different types of RF coils are used for transmission and reception, as is often the case in clinical scanners. To ease this implementation, it may be possible to prepare several types of ^{1}H pickup coils and transmit coils and make them interchangeable, so that they can be used in various devices. This issue may be mitigated to some extent

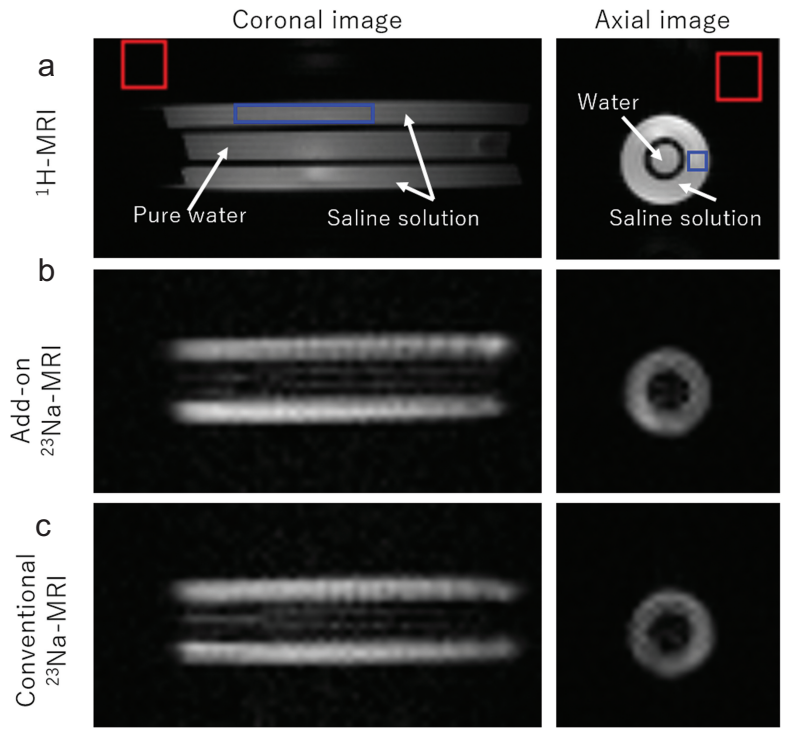

Fig. 8 ^{1}H-and ^{23}Na-MR images of the phantom. (**a**) ^{1}H-MR images. (**b**) ^{23}Na-MR images acquired with the add-on system. (**c**) ^{23}Na-MR images acquired with the conventional ^{23}Na-MRI system. The red and blue squares indicate the areas used for estimating the noise and signal levels.

Table 4 Image SNRs estimated from the saturated saline phantom images

System	SNR (coronal) (dB)	SNR (axial) (dB)
^{1}H-MRI system	42.0 (^{1}H)	45.2 (^{1}H)
Add-on system	32.5 (^{23}Na)	32.0 (^{23}Na)
Conventional ^{23}Na-MRI	32.6 (^{23}Na)	32.8 (^{23}Na)

for clinical ^{1}H-MRI scanners because there are not so many variations in coils supplied by vendors.

The second issue is the reproducibility of the sample (or subject) position. In this study, the magnet bore was very small compared with a clinical scanner. When the target configuration is switched from ^{1}H-MRI to the ^{23}Na-MRI system, the sample has to be removed from the RF coil, the add-on RF coil assembly inserted, and then the sample reinserted. This is not only time-consuming but also reduces the reproducibility of the sample location. However, if a clinical scanner that had a larger useable volume was employed, a more sophisticated platform that might have removable RF isolation shield could be designed. The positioning reproducibility should be better for all of the ^{1}H/^{23}Na overlay imaging.

Third problem is that of free space constriction: the free space in the ^{1}H-RF coil was reduced by installing the add-on RF coil assembly, consisting of the RF shield, pickup and transmit coils, and the ^{23}Na birdcage coil. This leads to a reduction in the available sample size and ^{1}H sensitivity. In this study, the free space in the coil was equivalent to 100 mm DSV when only the ^{1}H-RF coil was used, but when the add-on coil assembly was added, the free space was reduced to less than half of that. There is room for more improvement in the size and placement of these additional devices. For example, the use of flat, surface coils, instead of the ^{23}Na birdcage coil, might increase the free space. In contrast, for actual clinical ^{23}Na imaging, a transmission/receive ^{1}H coil, such as a birdcage head coil, could be used outside the B_0 magnetic field. In this setting, the ^{1}H transmission and receive head coils would be just a part of the RF signal transducer line, and therefore, the ^{1}H-RF isolation shield of this study could be smaller. The use of an RF shield with a thinner or smaller casing would also reduce the size of the add-on coil assembly. It is also possible to employ a normal setting of a clinical ^{1}H-MRI with a ^{1}H transmission coil and ^{1}H-receive only coils: a similar alignment of ^{23}Na coils and proper transfer of the receiving signals to each coupled ^{23}Na/^{1}H coils could be usable. A ^{23}Na sensitivity map could be made in the future. The reduced ^{1}H sensitivity would be compensated for by the use of a multichannel array coil with a large number of elements and flexible coil geometry, enabling the close fitting to an imaging object.

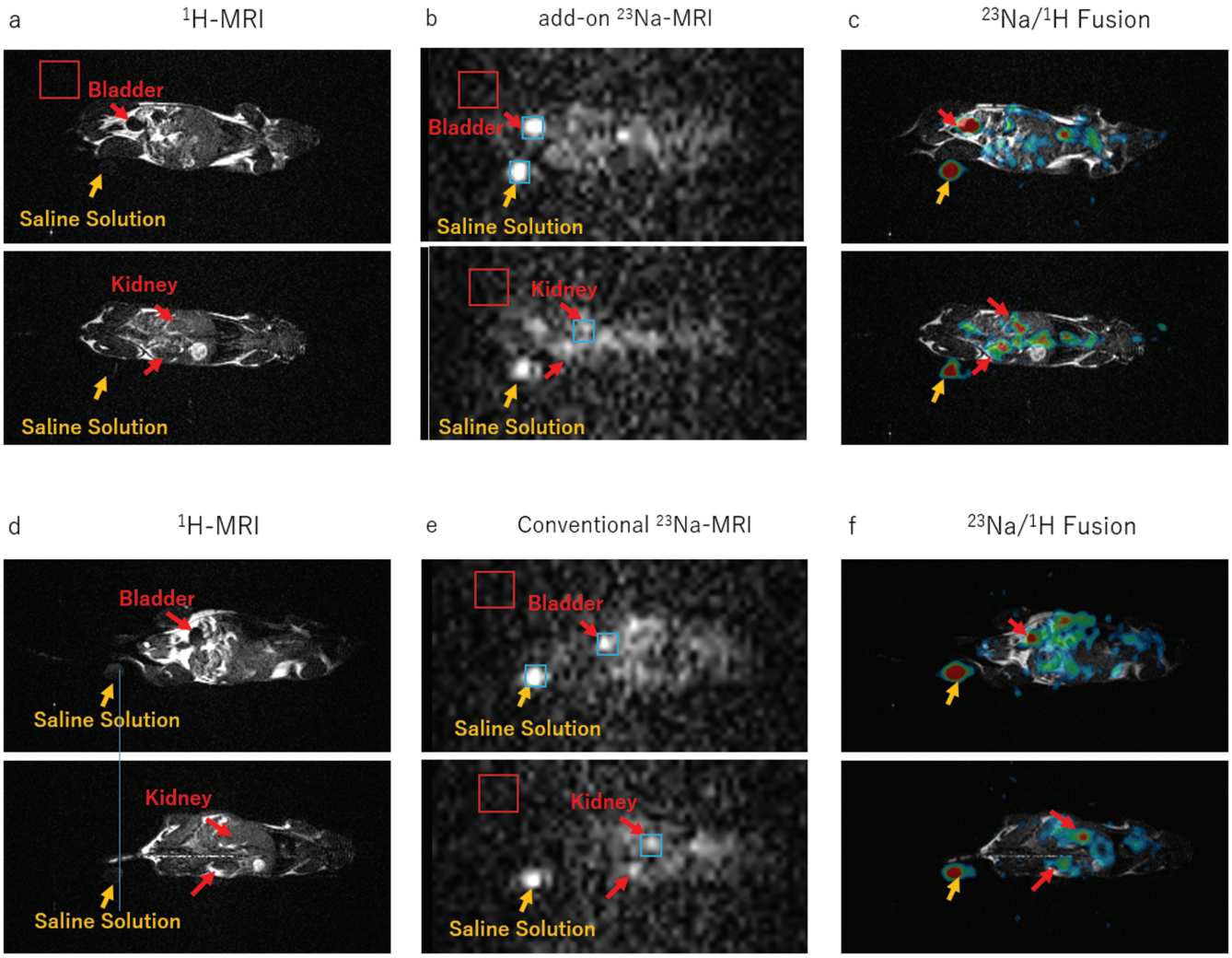

Fig. 9 ^{1}H- and ^{23}Na-MR images of the live mouse. (**a**) ^{1}H-MR images acquired with the 1H-MRI system. (**b**) ^{23}Na-MR images acquired with the add-on system. (**c**) Fusion images of (**a**) and (**b**). (**d**) ^{1}H-MR images acquired with the ^{1}H-MRI system. (**e**) ^{23}Na-MR images acquired with the conventional ^{23}Na system. (**f**) Fusion images of (**d**) and (**e**). The red and blue squares indicate the areas used for estimating the noise and signal levels, respectively.

Table 5 Image SNRs estimated from the mouse ^{23}Na images

System	Saline solution	Bladder	Kidney
Add-on system	19.8	19.9	15.1
Conventional ^{23}Na-MRI	18.3	20.3	14.2

The fourth concern is the implementation of short TE sequences. Whether it is possible to image with an extremely short TE depends on the performance of the parent ^{1}H-MRI system, the imaging sequence, and the specific delay of the add-on system. Of course, sequences that cannot be performed on the parent system are impossible to perform. Otherwise, the delay of the add-on system is quite short (a few microseconds), and standard sequences would be almost unaffected. However, sequences with extremely short TE, such as zero echo-time imaging, ultrashort TE imaging, and sweep imaging with Fourier transformation, might be affected.

Conclusion

In this paper, we proposed a new method for realizing ^{23}Na-MRI with minimal modifications to the standard ^{1}H MRI at minimal cost. Using the RF CBR, we have developed a prototype of an RF add-on ^{23}Na platform that can realize ^{23}Na-MRI by attaching to an existing ^{1}H-MRI system. The CBR generated the control signals for ^{23}Na-MRI with high fidelity. The performance of the add-on system was evaluated using phantom and *in vivo* studies. The add-on system provided ^{23}Na-MR images

with comparable image quality and SNR to the conventional ^{23}Na-MRI system, without modifying the scanner configuration. The concept of the proposed system is applicable to other conventional ^{1}H-MRI scanners and would provide the opportunity to assess the clinical and research applications of ^{23}Na -MRI.

Acknowledgments

This research was supported by Japan Agency for Medical Research and Development (AMED) under Grant Number JP20hm0102062.

Conflicts of Interest

Tomoyuki Haishi is an employment of MRTechnology Inc. The other authors declare that they have no conflicts of interest.

Supplementary Information

Supplementary files below are available online.

Optimization of configurations of pickup/transmit coil

The configurations of pickup/transmit coils were optimized in advance using a commercial electromagnetic simulator (FEKO, www.feko.info) in such a way that the transfer functions between the pickup coil and ^{1}H-RF coil and that between the transmit coil and ^{1}H-RF coil were maximized. The optimization was performed as follows. Let φ be the azimuth angle and l be the axial position of the center of the coil (Supplementary Fig. 1), the parameter ranges are listed in Supplementary Fig. 1. The object function for the pickup coil (or transmit coil) optimization was the transfer function between the pickup coil (or transmit coil) and the ^{1}H birdcage RF coil. An optimal solution (φ_{opt}, l_{opt}) with the maximum objective function was obtained by a particle swarm optimization algorithm.

The optimal solutions are listed in Supplementary Table 2. The pickup and transmit coils used in this study were constructed according to this optimization result. Supplementary Fig. 2 shows the S-parameters measured with the constructed coils.

Supplementary Fig. 1
Coil configuration.

Supplementary Fig. 2
S-parameters measured for the constructed pick-up, transmit, and ^{1}H birdcage RF coils. 1: pick-up coil; 2: transmit coil; 3: ^{1}H birdcage RF coil.

Supplementary Table 1
Search ranges for optimization.

Supplementary Table 2
Optimal solutions.

References

1. Hu R, Kleimaier D, Malzacher M, et al. X-nuclei imaging: Current state, technical challenges, and future directions. J Magn Reson Imaging 2020; 51:355–376.
2. Zöllner FG, Kalayciyan R, Chacón-Caldera J, et al. Pre-clinical functional magnetic resonance imaging part I: The kidney. Z Med Phys 2014; 24:286–306.
3. Zöllner FG, Konstandin S, Lommen J, et al. Quantitative sodium MRI of kidney. NMR Biomed 2016; 29:197–205.
4. Haneder S, Michaely HJ, Schoenberg SO, et al. Assessment of renal function after conformal radiotherapy and intensity-modulated radiotherapy by functional 1H-MRI and 23Na-MRI. Strahlenther Onkol 2012; 188:1146–1154.
5. Maril N, Rosen Y, Reynolds GH, et al. Sodium MRI of the human kidney at 3 Tesla. Magn Reson Med 2006; 56:1229–1234.
6. Shah NJ, Worthoff WA, Langen KJ. Imaging of sodium in the brain: a brief review. NMR Biomed 2016; 29:162–174.
7. Petracca M, Fleysher L, Oesingmann N, et al. Sodium MRI of multiple sclerosis. NMR Biomed 2016; 29:153–161.
8. Petracca M, Vancea RO, Fleysher L, et al. Brain intra- and extracellular sodium concentration in multiple sclerosis: a 7 T MRI study. Brain 2016; 139:795–806.
9. Dani KA, Warach S. Metabolic imaging of ischemic stroke: the present and future. AJNR Am J Neuroradiol 2014; 35(6 Suppl):S37-43.
10. Bottomley PA. Sodium MRI in human heart: a review. NMR Biomed 2016; 29:187–196.
11. Constantinides C. Cardiac multinuclear imaging. In: Constantinides C, ed. Protocols and methodologies in basic science and clinical cardiac MRI. Cham:Springer International Publishing, 2018; 215–236.
12. Umathum R, Rösler MB, Nagel AM. In vivo 39K MR imaging of human muscle and brain. Radiology 2013; 269:569–576.
13. Guermazi A, Alizai H, Crema MD, et al. Compositional MRI techniques for evaluation of cartilage degeneration in osteoarthritis. Osteoarthritis Cartilage 2015; 23:1639–1653.
14. Fitzsimmons JR, Beck BL, Brooker HR. Double resonant quadrature birdcage. Magn Reson Med 1993; 30:107–114.
15. Isaac G, DSchnall M, Lenkinski RE, et al. A design for a double-tuned birdcage coil for use in an integrated MRI/MRS examination, J Mag Reson 1969; 89:41–50.
16. Choi CH, Hong SM, Felder J, et al. The state-of-the-art and emerging design approaches of double-tuned RF coils for X-nuclei, brain MR imaging and spectroscopy: A review. Magn Reson Imaging 2020; 72:103–116.
17. Hashimoto S, Kose K, Haishi T. Comparison of analog and digital transceiver systems for MR imaging. Magn Reson Med Sci 2014; 13:285–291.
18. Lustig M, Donoho D, Pauly JM. Sparse MRI: The application of compressed sensing for rapid MR imaging. Magn Reson Med 2007; 58:1182–1195.
19. Near J, Bartha R. Quantitative sodium MRI of the mouse prostate. Magn Reson Med 2010; 63:822–827.